

“Decoding (urban) form and function using spatially explicit deep learning”

ABSTRACT: This paper advances our understanding of the extent to which conventional deep learning methods can be applied to satellite imagery to capture the composition of urbanised landscapes. The building blocks that make up those -the activities and agents conceptualised as urban function and the structure that supports them conceptualised as urban form- can be arranged in many ways. This paper relies on the concept of “spatial signatures”, a characterisation of space dependent on data released at a variable rate - an issue that could be resolved by remote sensing and satellite imagery. Using Sentinel-2 imagery, we explore this pathway within convolutional neural networks and predictive modelling trained to identify spatial signatures across Great Britain. While deep learning is established, its application has often ignored the geographical nature of the images. Our focus is to develop a performant model but also to learn about the effect of spatially explicit methods of doing so. The results indicate that classification of urban environments is more challenging than non-urban. However, when applying spatially explicit methods the accuracy is competitive with established models. This suggests that satellite imagery reflect form and function in greater detail than is usually present in available remote sensing products.

Key words: spatial signatures, classification, remote sensing, artificial intelligence, open data

1. Introduction

The way in which different urban functions are arranged within space, and the forms these give rise to, are important to understand how cities work, how they interact with the human and environmental systems that create them, and how policy can effectively intervene. Urban form and function matter, at least, for two reasons (Arribas-Bel and Fleischmann, 2022): first because cities use both to encode their history; and second because, once in place, the physical layout of functions within a city condition how it can and will develop in the future. A key requirement to understand form and function in cities is adequate measurement, which implies detailed, consistent, and scalable characterisations that can be updated frequently over time. These characteristics then allow not only to observe detail, but to see it unfold both over space and time. There is a large literature measuring these phenomena, and it is relatively common to find any two of those characteristics (i.e., detailed and consistent, consistent and scalable, and detailed and scalable) present in a given piece of work. Research bringing the three together is still rare, although some is emerging (e.g., Fleischmann and Arribas-Bel, 2022) thanks to the confluence of better data, open source software, and cheap computing power. Still, generating detailed, consistent, and scalable classifications of urban form and function is an expensive process that is difficult to refresh regularly because most of the underlying data sources only see updates infrequently.

A promising option to improve the frequency of these classifications is satellite imagery. Satellite technology has radically increased and improved the amount of data available on the Earth, and shows no signs of slowing down. More and better imagery has been complemented with the rise of new computer vision algorithms, such as deep learning (LeCun et al., 2015), that allow to extract more value from the same amount of data; and the availability of computing power that makes it possible to deploy them cheaply without the steep learning curve required only a few years ago. The convergence of these three trends in remote sensing is unlocking achievements that even very recently seemed beyond the realm of possibility. One such area is the use of remote sensing and satellite technology to decode complex patterns in urban landscapes, such as the spatial signature of different types of form and function. Just as importantly, many of these advances are being built atop technology developed under open licenses that allow to further build on them, freely redistributing downstream outputs.

The use of satellite technology for measuring different aspects of urban environments is by no means new. Much of the present work falls within the broad category of urban remote sensing (Rashed and Jürgens, 2010, Weng and Quattrochi, 2018, Yang, 2021). In fact, the promise of using remote sensing data to decode the complexity of urban structure has long been recognised (e.g., Longley, 2002). Much of the work in this area has traditionally focused on identification of individual geographic features, such as building footprints (e.g., Microsoft, 2019) or trees (e.g., Ke and Quackenbush, 2011). More recently, the field has started to pay increasing attention to the use of modern algorithms such as deep learning (Lai et al., 2021), and attempting to map more complex patterns that involve bundles of features rather than a single one (e.g., Kuffer et al., 2021). On the adjacent domain of Land Use / Land Cover (LULC) mapping, recent advances

have shown the potential of using frequently updated, open satellite data in combination with modern computer vision to effectively map land cover globally in quasi continuous ways (e.g., Karra et al., 2021, Brown et al., 2022; see Venter et al., 2022 for a detailed comparison of some of the most novel data products in this realm).

While most of the efforts in urban remote sensing have focused on the identification of individual features or single uses, much less work has been directed at decoding patterns that involve several features and/or uses to be identified. In some ways, the jump from the simpler goal of identifying one object or a single use to detecting a pattern that involves a particular bundle of them is not without its challenges and shortcomings (Wang et al., 2022b). But, given the performance of modern algorithms, and the increase in resolution and quality of even openly available imagery, realising this goal is starting to become possible. There are two areas that have received most of the attention in this context. One revolves around the prediction of Local Climate Zones (LCZs, Stewart and Oke, 2012). LCZs are a set of pre-defined classes of urban fabric originally developed for the study of the urban heat island effect. A growing body of literature has focused on developing more exhaustive and sophisticated models to extract these classes from satellite imagery (e.g., Koc et al., 2017, Wang et al., 2018b, Liu and Shi, 2020, Taubenböck et al., 2020, Zhou et al., 2021, 2022). The second one is focused on one particular type of urban form and function that is mostly found in regions which are typically data scarce: informal settlements, or urban slums. For the interested reader, Kuffer et al. (2016) provides an excellent starting point. Although much more in its infancy, a nascent area of interest is growing around using imagery to decode urban form (e.g., Wang et al., 2022a).

A common element of the recent advances reviewed above is the use of deep convolutional neural networks to perform the task of interest (i.e., classification/segmentation/recognition) from satellite imagery. Some studies, particularly those with sufficient data and computation available, train networks from scratch. These involves sometimes building a bespoke architecture (e.g., Othman et al., 2017), bespoke data for training (e.g., Qiu et al., 2020, Karra et al., 2021), or both (e.g., Taubenböck et al., 2020, Zhu et al., 2022, Sharma et al., 2017, Wang et al., 2018a). Other works however rely on existing architectures like VGG/16 (Simonyan and Zisserman, 2014), UNet (Ronneberger et al., 2015), or ResNet (He et al., 2016); standardised databases such as ImageNet (Russakovsky et al., 2015) for training; or both (e.g., Qiu et al., 2020, Karra et al., 2021, Srivastava et al., 2019). The latter is known as *transfer learning* and usually involves re-training of the top layers of the network to customise predictions to the specific use case, while retaining unchanged the original weights for all the other layers.

While deep learning has been recently introduced in the analysis of urban satellite imagery, its application has so far mostly ignored the geographical nature of the images being fed to these algorithms. This is not entirely unreasonable. Much of the state of the art in deep learning and computer vision was developed in the last decade with “aspatial imagery” in mind, in particular consumer photographs uploaded and shared through the internet (e.g., featuring cats and dogs). As such, many of the assumptions (e.g., unrelated images), tricks (e.g., data augmentation techniques), and limitations (e.g., shape of the input data) these models feature are intimately related to data of this kind. The application of deep learning to satellite imagery is

in what we consider a first phase in which cutting edge computer vision has been deployed to images that, rather than animals or people, represent locations on Earth observed from above. Because of the overall impressive performance of modern algorithms, the results are impressive, even with largely unmodified models. However, this does not imply there is no further margin for improvement.

With many existing methods, there is a tendency towards a simplification of urban environment. In the most simple cases, we can talk about differentiation between built-up areas and non-built-up land, occasionally expanded to a few gradual steps in between (e.g. degree of urbanization by Dijkstra et al. (2021)). Land use and land cover classifications focus primarily on non-urban landscape, leaving all patterns that make up cities in a handful of classes. LCZ classification is based on pre-defined conceptual classes designed with an RS application in mind, omitting distinctions that are not easy to see on imagery. The understanding on how many types of urban insight can be seen from above is still very much an unexplored area.

This paper advances our understanding of the extent to which deep learning methods can be applied to satellite imagery in order to capture the composition of primarily urbanized landscapes. It starts from an existing classification of Great Britain that is data-driven, designed to best capture urban form and function from available data (i.e. it is not designed to be seen on satellite imagery), and that flips the ratio of urban vs non-urban classes compared to most LULC classifications. From there, we move towards answering whether we can reliably detect this type and granularity of urban classification from open satellite imagery. Furthermore, given the geographical nature of the task, whether the scope for spatially-explicit methods built on top of the output of neural network to bridge the gap between computer vision and geography? Understanding these topics can potentially allow development of a time series of otherwise static classifications like the one used in this paper and uncover the evolution of urban form and function in cities. The remainder of the paper is structured as follows: Section 2 describes the data we use as well as the methodological strategy we follow; Section 3 presents the key results from our experiments; and Section 4 discusses their relevance and concludes.

2. Materials and Methods

In this section, we present the materials used in the research - the British spatial signatures we would like to identify and Sentinel 2 satellite imagery - and methods designed to understand our ability to train a conventional model on such a task and to unpack the role of geography in image-based deep learning.

2.1 Materials

The research uses only two data inputs, one representing the "ground truth" we aim to predict using neural networks and the other representing satellite imagery. While the latter does not need much introduction, the British spatial signatures used as labels need to be explained further.

2.1.1 British Spatial Signatures

Spatial signatures are a classification of space covering the entirety of a case study area. They are defined as "*a characterisation of space based on form and function designed to understand urban environments*" (Arribas-Bel and Fleischmann, 2022, p.4). This definition points at the clear distinction between signatures and traditional LULC classifications. Taking the example of CORINE (European Environment Agency, 1990) as a representative of LULC, it has 44 distinct classes, out of which 2 cover urban form, and six other can be loosely related to urban areas¹. A similar situation arises with recently released global LULC datasets. European Space Agency's WorldCover project distinguishes 11 classes, of which one is urban (Built-up) (Zanaga et al., 2021). Esri's Land cover has 9 classes: one is *Built Area*, and the rest covers unbuilt areas (Karra et al., 2021). This ratio of built vs unbuilt classes is typical but not very suited for research applications focusing on urban environments. Spatial signatures invert this ratio as they are primarily classifying urban space as illustrated visually in Figure 1. That is one of the main reasons for the existence of spatial signatures. There are very few data products that focus on the classification of the internal organisation of cities as a combination of the physical form and the function of space. Even if they do, they are often limited by detail, granularity, or the geographical extent of the area they cover. Spatial signatures are designed to overcome these limitations.

The focus on urban environments is shared with the notion of *urban functional zones* (Lu et al., 2022, Izzo et al., 2022, Jing et al., 2022), though the latter is more focused on the function of urban space, while spatial signatures explicitly capture also form, leading to a set of categories that go beyond "residential", "industrial", or "commercial" categories, and provide a more nuanced characterization of space.

As illustrated in Arribas-Bel and Fleischmann (2022), spatial signatures are by far not limited to the context of Great Britain or similarly data-rich countries. The method presented in this paper is expected to apply to any area where spatial signature classification is available or can be generated.

There are two main concepts embedded in spatial signatures delivering urban-focused classification. The first one is the spatial unit called the enclosed tessellation cell (ETC). To derive ETCs, Arribas-Bel and Fleischmann (2022) first generate *enclosures*, spaces fully enclosed by a set of barriers (roads, railways, rivers, coastline). ETCs are an outcome of Voronoi tessellation based on building footprint polygons. The resulting spatial unit has adaptive granularity reflecting the scale of each urban pattern. The second is the selection of characters describing each ETC. They measure form and function, primarily urban phenomena and mostly omit environmental aspects focusing on land cover patterns. However, spatial signatures depend on a wide range of data inputs that are being updated at a variable rate. Some in monthly snapshots but others, based on census data, only every ten years. Given this heterogeneity, it is nearly impossible to provide a consistent yearly time series of their evolution. This is where remote sensing based on satellite imagery may help.

¹Continuous urban fabric, Discontinuous urban fabric; Construction sites, Green urban areas, Sport and leisure facilities, Industrial or commercial units, Road and rail networks and associated land, Port areas

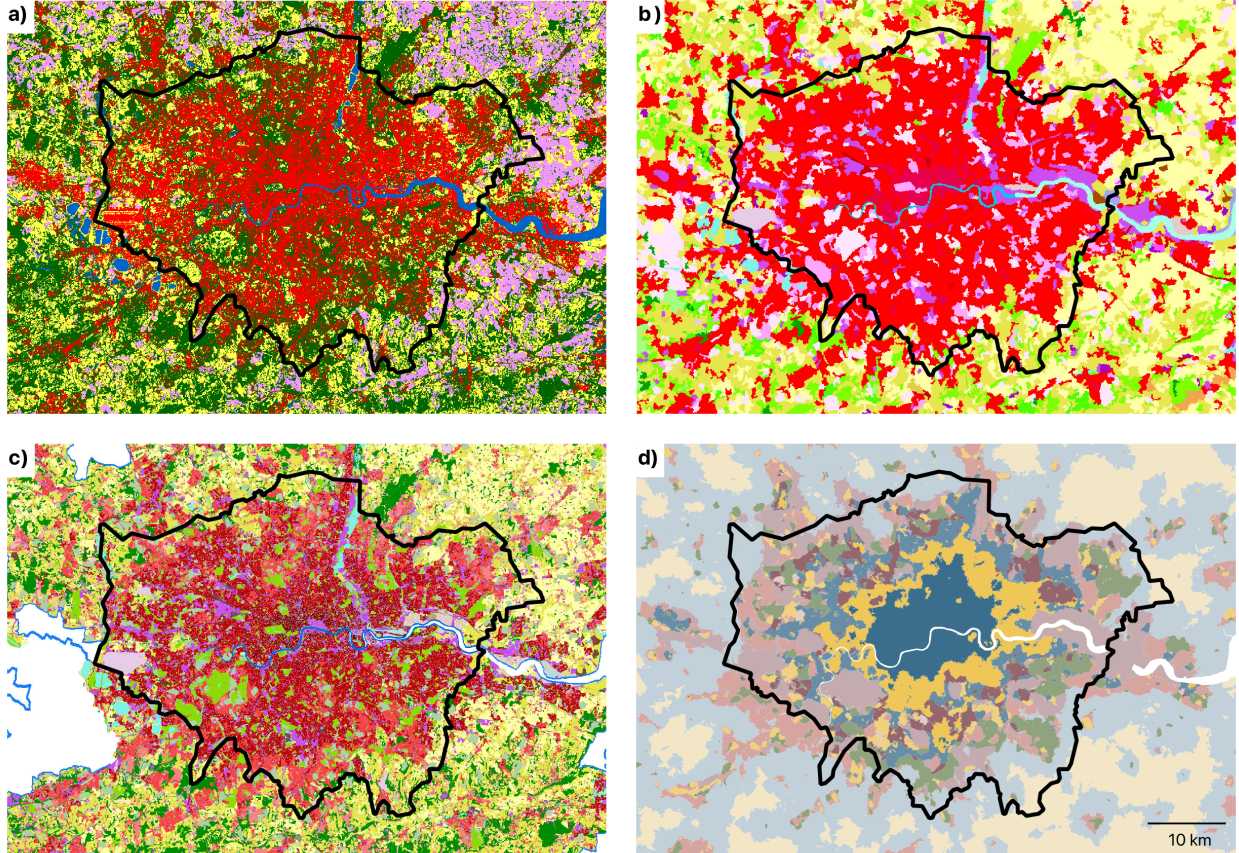


Figure 1: A visual comparison between established LULC products and spatial signatures. Panel a) shows the WorldCover classification by ESA (Zanaga et al., 2021), panel b) shows the CORINE land cover classification (European Environment Agency, 1990), panel c) shows the Copernicus Urban Atlas (European Environment Agency and European Environment Agency, 2020), and panel d) shows the British spatial signatures (Fleischmann and Arribas-Bel, 2022). The latter is the focus of this paper. The direct comparison showcases the major difference between the conceptualisation of urban areas between different classifications, with traditional LULC providing only a minimal distinction between types of urban development, whilst spatial signatures provide a much more nuanced view, allowing a different type of understanding of the environment.

Signature type	area (sq.km)	ETC count	area (%)	ETCs (%)
Countryside agriculture	93,856.1	3,022,385	41	21
Accessible suburbia	2,244.5	1,962,830	1	14
Dense residential neighbourhoods	957.2	502,835	0	3
Connected residential neighbourhoods	565.4	374,090	0	3
Dense urban neighbourhoods	570.6	238,639	0	2
Open sprawl	5,081.5	2,561,211	2	18
Wild countryside	91,306.3	595,902	40	4
Warehouse/Park land	2,462.4	707,211	1	5
Gridded residential quarters	261.2	209,959	0	1
Urban buffer	31,588.8	3,686,554	14	25
Disconnected suburbia	708.9	564,318	0	4
Local urbanity*	231.1	86,380	0	1
Concentrated urbanity*	7.8	1,390	0	0
Regional urbanity*	76.4	21,760	0	0
Metropolitan urbanity*	16.5	3,739	0	0
Hyper concentrated urbanity*	2.2	264	0	0

Table 1: Classes of British spatial signatures and their coverage in terms of area and a number of ETCs. Urbanity classes marked with * are combined for the experiments presented in this paper.

As presented in Fleischmann and Arribas-Bel (2022), British spatial signatures are one application of the concept of spatial signatures in the context of Great Britain. It divides the space into the 16 data-driven classes (Figure 2) listed in Table 1. Out of these 16 classes, nine are entirely urban, four are peripheral, and only three classify natural spaces, inverting the ratio of built vs unbuilt classes common in LULC. However, out of these 16 classes, some are very rare, and it would not be feasible to attempt to predict them. Therefore, we merge five classes under the “urbanity” group into a single one and use the resulting 12 classes throughout this paper, while using entirety of Great Britain as a study area. A note of caution on the delineation of these classes is warranted. While maps like those in Figure 2 implicitly convey the idea of clearcut boundaries between signature types, reality is much more complex. Thus, boundaries between signatures should be taken as Fleischmann and Arribas-Bel (2022)’s best estimate at delineating each area, but also on the understanding that reality is much more fluid, porous, and fuzzy.

2.1.2 Sentinel 2 imagery

The second data input used in this research is satellite imagery provided by the Sentinel 2 mission. Specifically, we use the pre-processed cloud-free mosaic of Sentinel 2 released by Corbane et al. (2020). The mosaic provides pixel-level composite based on imagery for the period January 2017–December 2018 at an original resolution of 10 meters per pixel. While Sentinel 2 captures many spectral bands beyond traditional visible red, green and blue (RGB), this research uses only RGB bands due to its employment of pre-trained neural networks stemming from non-satellite imagery that is composed only of RGB and an attempt to minimize training from scratch that would need to happen to derive weights for other bands. The exclusion of other bands may be seen as a

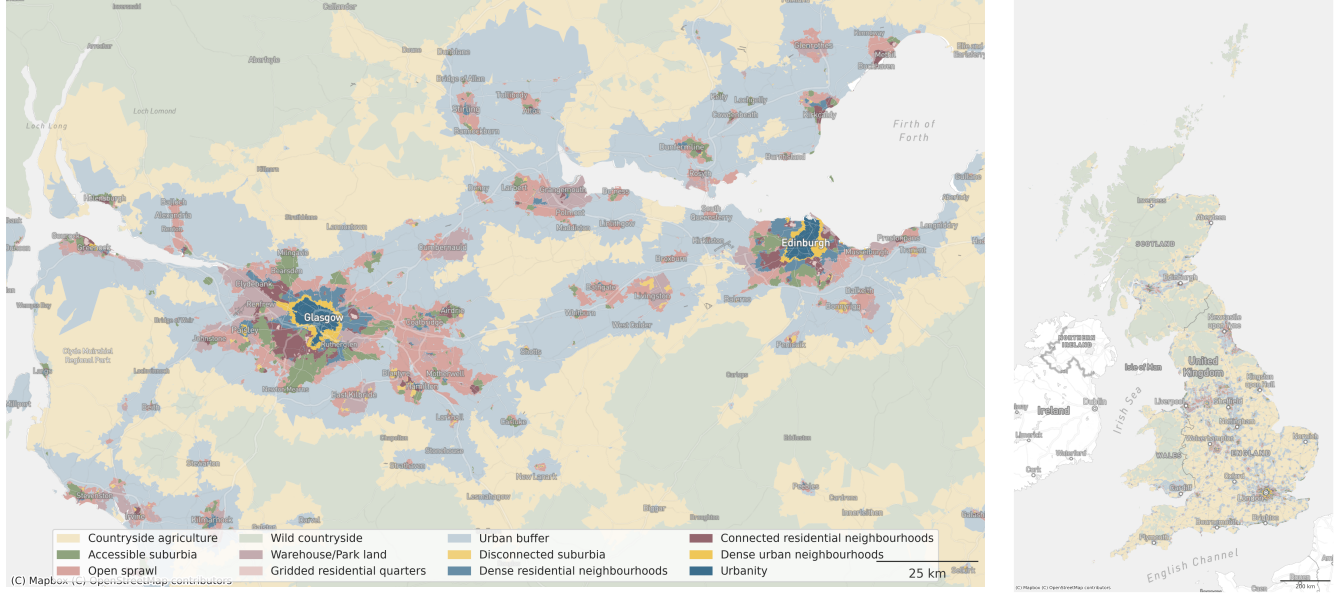


Figure 2: Spatial signatures in the full extent of Great Britain (right) and zoomed to a metropolitan area of the Scottish Central Belt stretching from Glasgow to Edinburgh (left), limited to 12 classes used in this paper.

limiting factor of the work, but we believe that, as with other aspects that will be discussed later, it efficiently illustrates the *lower bound* of the performance of the presented method and can be only improved with the addition of other spectral bands or other data (e.g. synthetic-aperture radar imagery).

Another notable aspect of the Sentinel 2 imagery is the resolution. Ten meters per pixel may be enough to distinguish LULC classes, as shown by the examples discussed above. However, it is unclear whether it is enough to delineate types of urban environments. Individual buildings often do not stretch beyond the spatial extent of two pixels, which is severely limiting what we can *see* on the image, as illustrated in Figure 3. While other data sources may provide better resolution², potentially improving model performance, this research is bound within the limits of *open data*, where Sentinel 2 is the best offering to date.

2.2 Methods

We define our challenge as an image classification task and use competing alternatives to explore which one performs best and to assess whether the *best* is good enough. Each of them implies geographically relevant trade-offs. First, we build and train a model composed of a convolutional neural network and probability modelling able to predict the 12 classes derived from the spatial signatures. Second, we use methods designed to unveil which of the inherently geographical decisions being tested has a significant effect on the resulting performance and should therefore be considered when applying CNN to spatial problems.

²For example, commercial imagery by Maxar reaches a resolution of 30cm per pixel and imagery by Planet of 50cm per pixel

When selecting the CNN architecture, we have intentionally excluded image segmentation. While it seems like an ideal candidate for the task at hand, there are several reasons for its exclusion. The first has to do with the spatial signatures and the nature of the boundaries between individual types. While the dataset from Fleischmann and Arribas-Bel (2022) delineates them with hard boundaries when one cell is a type A and the neighbouring one a type B, the reality is not that simple, and these boundaries should be treated more as a fuzzy edge than the hard one. There is very rarely an immediate switch between one type of urban environment and the other one. In many cities, two types tend to form a transition on the edges where neither is dominant. A situation like this is very challenging for the image segmentation as it often looks at delineation of water bodies, buildings or other precisely defined patches on an image. The second reason is that the image segmentation, having a prediction for individual pixels, would not allow us to use the second part of the method and test the effect of spatial lag in modelling efficiently. The only way of doing that would be to run the experiment on a pixel level which would be extremely computationally expensive, hence challenging to reproduce. We believe that the method that can be run on a local machine is in the end, more valuable than the one requiring a high-performance cluster.

Overall, our exercise is structured as a comparison of models that attempt to predict the 12 spatial signatures entirely from Sentinel 2 imagery. Each model 1) takes a set of training data as input; 2) runs the class prediction using the convolutional neural network (CNN); and 3) builds a (spatial) model on top of the resulting probabilities. The differences between the models are capturing the geographical options that are being tested: extent of the area sampled from the satellite imagery into a single *chip*, presence of spatial augmentation, class exclusivity within each chip, and an architecture of probability modelling on top of a prediction coming from the CNN. Finally, the performance of each model is assessed using both traditional non-spatial techniques used in deep learning and bespoke spatial metrics. Given a large number of resulting values, a regression approach is used to determine the effect of the tested options. Each of the steps is further discussed in detail in the subsequent sections.

2.2.1 Chip size

The first question that needs to be answered when trying to apply a classification algorithm on satellite imagery that spans a large amount of continuous land is how to sample such data into individual patches (or, hereafter, chips) that can be assigned to classes. Pre-trained CNNs usually expect a square image of a certain size, but that does not mean that the same size (in terms of pixels) needs to be directly sampled from the image, thanks to possible resampling. What should be retained, though, is the ratio. Therefore, we need to sample square chips of a custom size. Within an image classification framework, which is the first type of model that is tested, we assume that each chip contains data of a single class only. Therefore, such a chip should be entirely within the boundary of a single signature type. That poses some restrictions as spatial signatures, especially in the urban context, tend to be relatively granular, and large chips would not fit inside the boundaries, reducing the number of valid chips for training. Therefore, the goal is to find a balance between the number of chips sampled from the data and the amount

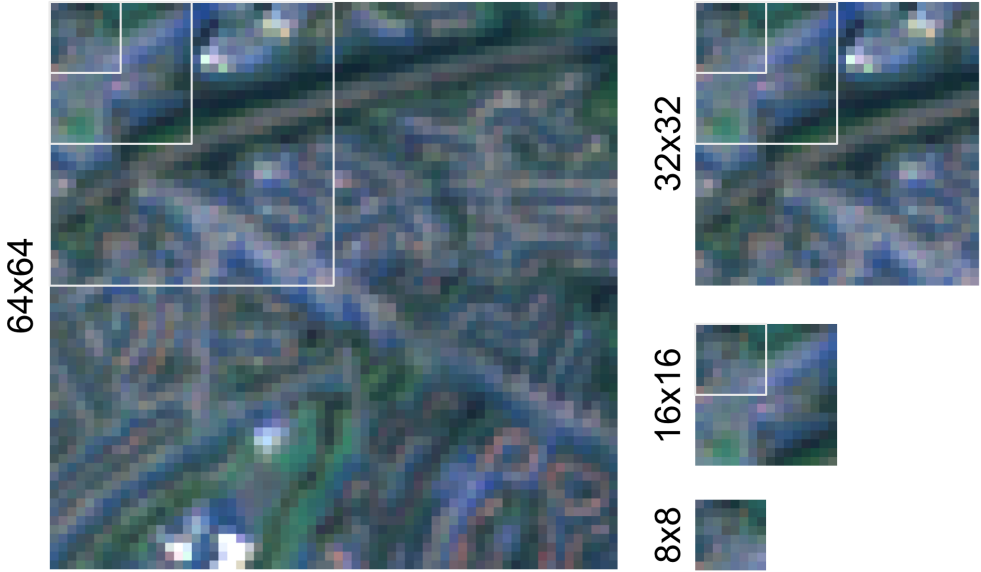


Figure 3: Illustration of the selected chip sizes using the Sentinel 2 cloud-free mosaic. Each of the chips also shows the sizes of the smaller options as a white outline.

of information each chip can hold. Given the relatively coarse resolution of Sentinel 2, a chip of 100x100 meters consists of only 10x10 pixels, which may not be enough to capture the nature of a signature type and distinguish it from other types. On the other hand, a chip of 1000x1000 meters, which is likely large enough to capture the difference, will not fit in most of the signature boundaries and we would end up with only a few chips per urban class.

The literature rarely discusses the decisions involved in defining the chip size for single-class chip classification. In some cases, the size is predetermined due to the requirement of either a pre-trained model or an existing set of labelled data (Taubenböck et al., 2020). In others, the size that has been used in previous studies is applied again without discussing the implications of such a decision (Wang et al., 2018b). From a spatial analysis perspective, this approach is surprising as deciding the chip size is a prime example of the modifiable areal unit problem (also known as MAUP, Openshaw, 1981), especially the aspect about scale, which states that a change of the scale may affect the outcome of an experiment. Hence such an effect should be at least considered in an interpretation if not minimized where possible.

In this work, we try to understand the effect of chip size by testing all the models based on four different chip sizes - 80, 160, 320 and 640 meters representing chips of 8x8, 16x16, 32x32 and 64x64 pixels, respectively, illustrated on a Figure 3 and a Supplementary Figure 13.

2.2.2 (Spatial) data augmentation - Sliding

As mentioned above, in combination with the signature geometry and the requirement to keep chips exclusively within a single class, specific chip sizes may result in insufficient training data for some signature types causing imbalance in the training set. Under-sampling like this one can be a serious problem that is not unique to spatial modelling. However, traditional augmentation methods are not directly applicable here. For example, in an image classification problem trying

to determine if there is a cat or a dog on an image, we add some rotation or zoom to get more versions of the same image and expand the set of training data. Neither of these methods is applicable to spatial problems. Rotating the image would break natural light conditions, while zooming in would change the scale of the urban environment we attempt to capture. Moreover, distinction between some signature types is partially in different orientation of streets, rendering rotation-based augmentation counter-productive.

At the same time, the geographical and continuous nature of the data at hand allows us to use explicitly spatial augmentation techniques such as the one we call *sliding*. Sliding can be seen as overlapping sampling. Instead of overlaying a grid of chips over target geometry and using each pixel only once, we take the initial grid and slide it a few pixels horizontally and vertically, as illustrated in Figure 4. If the boundary of a slid chip is fully within a signature geometry, it is added to the pool of chips to be used. This process is done repeatedly to ensure that each class has a reasonable amount of chips to work with, while chips from the large signature types are intentionally undersampled to retain a relative balance between the classes in the training data.

It is to be noted that sliding can cause data leakage (sequences of pixels being present in both training and validation) if done before splitting the data into training and validation subsets. Therefore, we first create the initial grid, subdivide it spatially into four parts (40% for CNN training, 10% for CNN validation, 40% for probability modelling training, 10% for probability modelling validation) and apply sliding within each part to avoid any pixels being shared among chips from different sets. Subdivision into the four parts is done within each signature geometry to avoid potential geographical bias.

2.2.3 Model architecture

Model architecture refers to the analytical pipeline that transforms chips into a prediction for a single signature type. Our competing architectures contain two main parts. First is a CNN that transforms a single chip into a set of 12 probabilities, one for each signature type. Second is a mathematical function that converts such probabilities (considering only those for the chip of interest or in conjunction with those of neighbouring chips) into a prediction for a single signature type. This section describes each of these in detail. We would like to highlight that, contrary to the majority of deep learning-focused research, our focus is not on the architecture of the CNN itself. We assume the effect of geographic choices will largely show similar behaviour irrespective of the network architecture. For that reason, throughout our experiments we use EfficientNetB4 (Tan and Le, 2019), pre-trained on the popular ImageNet dataset (Deng et al., 2009). Appendix A. shows a brief comparison of several standard neural network architectures with a subset different hyperparameters and their performance on a subset of data to motivate our decision. The final selection of hyperparameters and top layers - 256 neurons using GlobalAveragePooling2D with a learning rate of 0.001 - is based on the global accuracy and models (re-)trained on a subset of the data. We then apply transfer learning by re-training the top layer of the pre-trained model and replacing it by a custom sequence of dense layers described below.

We consider three variants of the CNN. The default approach (which we will refer to *bic*, for “baseline image classification”) is a standard image classification problem, using the sets of chips

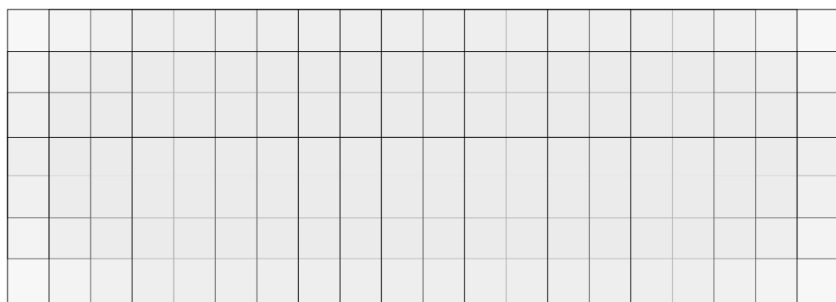
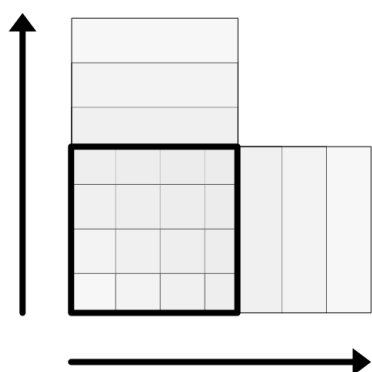
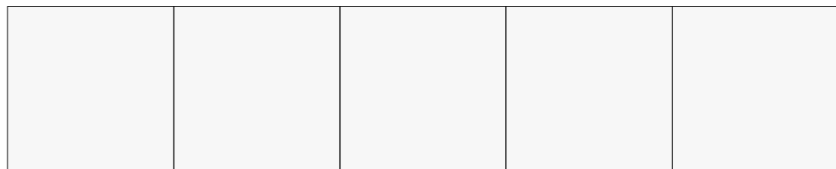


Figure 4: Diagram illustrating the sliding mechanism. The first row shows the initial non-overlapping grid, the last one final overlapping set of chips.

that are fully within a single signature type. The custom top layer of the pre-trained CNN then contains a Global Average Pooling (2D) layer, a dense layer with ReLu activation and 256 neurons, and a dense layer with the softmax activation and a number of neurons equal to a number of classes (12). The result for a single chip is a collection of 12 probabilities of a chip belonging to each signature type. The sum of all probabilities is one. An extension of this approach (*sic*, for “sliding image classification”) applies this technique to the data being spatially augmented with the sliding technique described above.

Our third approach recasts the image classification task as a multiclass prediction. If we relax the requirement that every chip is fully within the boundaries of a single signature type, we end up with many more available chips, but now some of them include more than a single label within their extent. Instead of a single label per chip, we now deal with a 1-D array of them. This can be beneficial from the geographical perspective as such chips now inherently encode the co-location of individual signature types and a model could use this information during the prediction. As signature types usually tend to neighbour only a subset of other classes (e.g., Urbanity never neighbours Wild Countryside), we can assume that information on co-location can positively impact predictive performance. We then include a set of chips sampled from a grid crossing the boundaries of signature types (using the same chip sizes as before) and adapt the CNN to perform multi-output regression (*mor*) instead of image classification. This change implies the top layer is now composed of a Global Average Pooling (2D) layer, a dense layer with ReLu activation and 256 neurons, and a dense layer with the sigmoid activation and a number of neurons equal to a number of classes (i.e., 12). The result for a single chip is a similar collection of probabilities, but these are now predicted proportions. As such, the sum of all of them ranges between 0 and 12 rather than between 0 and 1.

A comparison of the total number of chips used by each CNN is available in the supplementary table 7. The split of chips is then 40% for CNN training, 10% for CNN validation, 40% for probability modelling training, 10% for probability modelling validation equally across all the options. All CNN models are trained using the following hyperparameters: number of epochs: 200, optimizer: Adam, patience: 5, and a batch size: 32. See the relevant code in the linked repository for details.

The second step in the pipeline takes chip probabilities and turns them into predictions of a signature type. To do this, we compare five approaches of differing complexity and sophistication. These five variants stem from the combination of two components: the set of inputs used to make the prediction and the function transforming them into a single signature type. For a given chip i , we can express this step of the pipeline mathematically as follows:

$$S_i = f(P)$$

$$P = \underbrace{\sum_k P_{k-i}}_{\text{baseline}} \left[+ \underbrace{\sum_k \sum_{j=1}^{N-1} w_{ij} P_{k-j}}_{\text{wx}} \right] \quad (1)$$

where S_i is the prediction for the signature type of chip i (one of the k available types, where $k = 12$ in our empirical case, see Section 2.1.1) and $f(\cdot)$ is a function that transforms the inputs P

into S_i . The five approaches we compare derive from the different implementations of $f(\cdot)$ and P . On the latter, we compare models that only use P_{k-i} (probability that chip i is of type k) generated by the CNN for chip i (baseline) with alternatives (signalled with the wx term) that, in addition, also include an average of P_{k-j} (probability that chip j is of type k), which are the probabilities generated by the CNN for each neighbour j of chip i . This is akin to what in spatial analysis is called the *spatial lag* of each probability, and is calculated using a spatial weights matrix W that records the spatial relationship between every chip in the set. In our W , two neighboring locations i and j will receive a weight $w_{ij} = 1$, if they are in the same of the four split sets as defined above, and if they either are geographically contiguous or are nearest neighbours; while otherwise they will be considered non-neighbours and receive a weight $w_{ij} = 0$. To obtain an average of the neighbors, we row-standardise W so that $\sum_j w_{ij} = 1$. The second dimension other than P we vary is the function $f(\cdot)$ that maps it to the prediction S_i . We take three distinct approaches here: simply picking the maximum probability (`maxprob`), which we only use without the spatial lag of probabilities; an ensemble of binary logit models to predict each class (`logite`), then selecting the class with top probability, which we also use with the wx variant; and a histogram-based gradient boosted classifiers inspired by LightGMB (Ke et al., 2017) and implemented in `scikit-learn` (Pedregosa et al., 2011). This yields our five competing models: `maxprob`, `logite_baseline`, `logite_baseline-wx`, `HGBC_baseline`, and `HGBC_baseline-wx`.

2.2.4 Performance metrics

The goal of our experiments is to compare different models under varying geographical conditions to learn both which performs best, but also how different choices of geographical nature influence the overall performance when predicting form and function from satellite imagery. To provide a workbench that systematically compares each model and setup, we use a set of performance scores that operate either at the global or class level, and that measure performance in the traditional machine learning sense, as well as in the spatial sense.

We use four standard performance scores. *Cohen's kappa* score (κ , Cohen, 1960) is a measure of agreement between two sets of categorical labels that ranges from -1 to 1. Intuitively, it measures the extent to which the two sets agree with each other (i.e., same label for the same observation) beyond what would be expected from pure chance ($\kappa = 0$). Cases where there is more disagreement than expected from chance receive a negative score. *Global (within-class) accuracy* captures the proportion of observations correctly predicted (in a given class). The *Macro F1* is a score that aggregates class-based F1 scores. The F1 is the harmonic mean between precision (proportion of chips predicted in one class actually belonging to that class) and recall (proportion of chips belonging to a given class being predicted as such). We use both the *weighted Macro F1* as well as the *averaged Macro F1*. The latter takes the standard mean of the F1 scores for each class, while the former weights each F1 by the proportion of chips in each class.

In addition to traditional performance scores, we also evaluate how similar the spatial pattern of predictions is to that of the original labels. The measures described above are all “spatially unaware” in the sense that they quantify different aspects of the correctness of a model’s predictions but ignore their spatial patterning. Two sets of results may have the same amount of correct

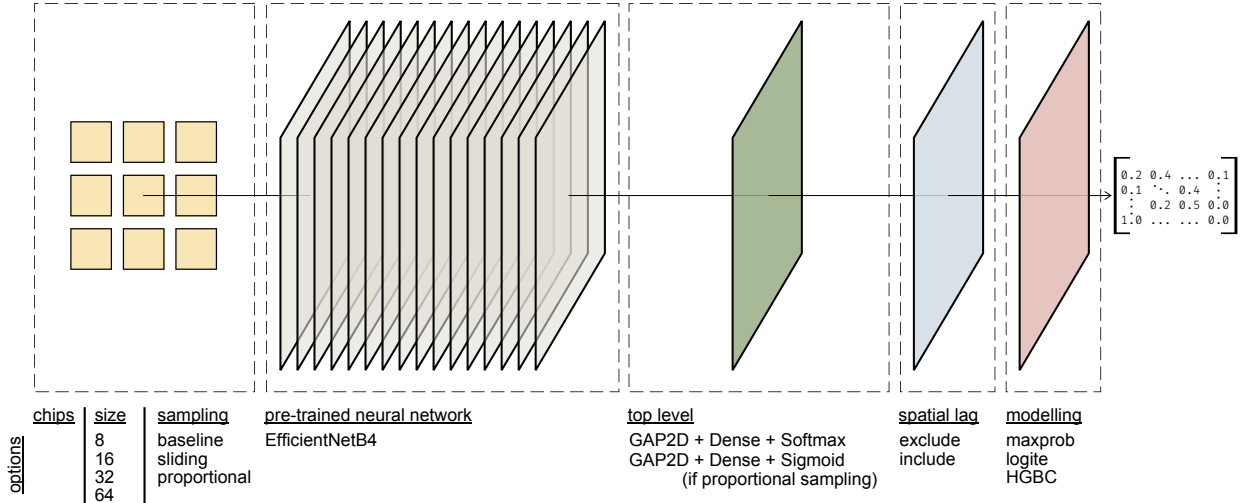


Figure 5: Model architecture overview.

predictions, but in one, the spatial layout of such predictions may be close to that of the observed labels, while the other one spatially allocates mispredictions in a way that differs more from what is observed empirically. Given the nature of our classification challenge –identify form and function over space from satellite imagery– the spatial dimension of model performance is of great importance. Since the spatial signatures represent a set of (12) distinct categories, we rely on the *join counts* statistic (JC, Cliff and Ord, 1981). The JC measures the degree of spatial concentration in a binary categorical variable; hence, we use it at the class level. For each class in each model, we retain the proportion of pairs of chips in the same class that are spatial neighbours (“joins”) over the total number of pairs that are spatial neighbours. Our neighbourhood definition relies on two alternative spatial weights matrices: one based on a distance threshold of 1Km (W_{thr}), and one that combines the nearest neighbour with those defined by contiguity (W_{union}). Our metric of interest is then the error (i.e., absolute value of the difference) between this proportion for the model of interest and that of the observed labels.

2.2.5 Summarizing experiments

The setup described above generates over 60 different models to be trained to predict 12 signature types and six performance measures to evaluate them. Making sense of their results requires a systematic approach that summarises them and provides explicit tests for the questions we are trying to answer. We achieve this goal by fitting linear regressions that explain performance scores for each model as a function of the characteristics of the setup evaluated. Specifically, we estimate the following two equations. First, for global metrics, we run:

$$Perf_r = \alpha + \sum_m \delta_m M_r + \sum_a \gamma_a A_r + \beta_1 Chip\ Size_r + \beta_2 W_r + \epsilon_r \quad (2)$$

where $Perf_i$ is each of our four global performance scores measured for trained model in setup i ; α is an intercept; M_i are indicator variables for the type of model we estimate (i.e.,

`maxprob`, `logite`, `HGBC`);³ A_i are similarly, indicator variables for the architecture used (i.e., `bic`, `sic`, `mor`);⁴ $Chip\ Size_i$ captures the number of pixels the chips in the setup contain; W_s is another indicator variable that takes the value of one if the model includes the spatial lag of signature type probabilities and zero otherwise; and $\epsilon_i \sim \mathcal{N}(0, \sigma)$ is an i.i.d. error term.

Second, for class-based scores, we fit:

$$Perf_{r-s} = \alpha + \sum_m \delta_m M_r + \sum_a \gamma_a A_r + \beta_1 Chip\ Size_r + \beta_2 W_r + \beta_3 [\%] Obs_{r-s} + \sum_s \zeta_s S_{r-s} + \epsilon_{r-s} \quad (3)$$

where $[\%] Obs$ represents either the number of chips in signature s in setup i or as a proportion of the total; and S_{i-s} an indicator variable for the signature type s ;⁵ and the rest is as in Equation 2. Importantly for both equations, $\delta_m/\gamma_a/\beta_1/\beta_2/\beta_3/\zeta_s$, parameters to be estimated by the regression model, provide a direct and formal test to the key questions we set out to answer with our experiments.

3. Results

Global accuracy

Global accuracy is shown in Table 2. It may seem that the results are underwhelming but taking a closer look, it is true only for some models, usually using smaller chip sizes and simpler architecture. Out of 60 tested models, 14 have global accuracy over 0.5, 6 over 0.6 and one over 0.7. Compared to the relevant metrics from established LULC models, Venter et al., 2022 reports that ESRI’s Land Cover reaches global accuracy of .75, Google’s Dynamic World 0.71 and ESA’s World Cover 0.65, rendering our highest performing models at par with these. However, they do perform considerably worse than established LCZ models, that report global accuracy of 0.87 (Taubenböck et al., 2020). Yet, this difference is expected as LCZ classes are designed with remote sensing in mind while spatial signatures aim to reflect the form and function independent of whether the distinction between two signature types shall be seen from satellite imagery. Nevertheless, global accuracy is far from providing the full picture.

Within-class accuracy

Within-class accuracy by the model can be seen in Figure 6 (a sister figure where scores are grouped by signature rather than by model can be found in Appendix B.). We notice some consistent patterns already. The baseline image classification (`bic`) tends to underperform other architectures, especially on more urban signature types. On the other hand, multi-output regression (`mor`), and using the larger chip size (32 or 64), tends to show the highest values across signature types and models. If we look at accuracy for individual signature types, both extremes (urbanity on one side and both countryside classes on the other) tend to be the easiest to predict.

³We remove HGBC to avoid perfect collinearity and hence treat it as the reference model.

⁴We remove BIC to avoid perfect collinearity and hence treat it as the reference model.

⁵We remove Accessible suburbia to avoid perfect collinearity and hence treat it as the reference model.

	Chip Size	B.I.C.	S.I.C	M.O.R
maxprob	8	0.30	0.32	0.29
	16	0.27	0.35	0.28
	32	0.42	0.34	0.35
	64	0.50	0.46	0.58
logite	8	0.32	0.35	0.31
	16	0.36	0.36	0.31
	32	0.46	0.36	0.36
	64	0.60	0.47	0.58
logite-wx	8	0.34	0.41	0.33
	16	0.42	0.46	0.33
	32	0.52	0.48	0.39
	64	0.67	0.55	0.59
HistGradientBoostingClassifier	8	0.32	0.36	0.32
	16	0.37	0.37	0.33
	32	0.48	0.40	0.49
	64	0.62	0.48	0.71
HistGradientBoostingClassifier-wx	8	0.35	0.44	0.35
	16	0.44	0.47	0.34
	32	0.54	0.50	0.40
	64	0.68	0.56	0.63

Table 2: Global accuracy of all the models tested in this study. Values higher than 0.5 are highlighted in italic, values higher than 0.6 in bold and a value over 0.7 in bold italic.

Regarding the models, there is no immediate conclusion to be made apart from a clear indication that the maximum probability (`maxprob`) approach is generally worse than any of the modelling, suggesting that there is a value in the modelling step. The within-class accuracy can be further explored using confusion matrices available in Appendix C..

Regression outputs for global performance metrics

Whilst plotting the accuracy is a way to build an intuition about the performance of individual options, it does not quantify their effects. The linear regressions shown in tables 3 and 4 provide better insight. The first regression explains global performance scores (Cohen’s kappa, Global Accuracy, Marco F1 weighted and Macro F1 average). We can draw a few conclusions from this. First, the chip size seems to have a positive effect on the results, as it is consistently significant across all metrics. Except for the average macro F1 score, there is a positive effect of the inclusion of spatial lag in the modelling step (W). Regarding the CNN step, we do not see a lot of significance but there are indications that sliding image classification and multi-output regression approaches outperform baseline image classification. Comparing the probability modelling step, we see an indication that the maximum probability is the least performant of the options, again suggesting the value of post-CNN modelling.

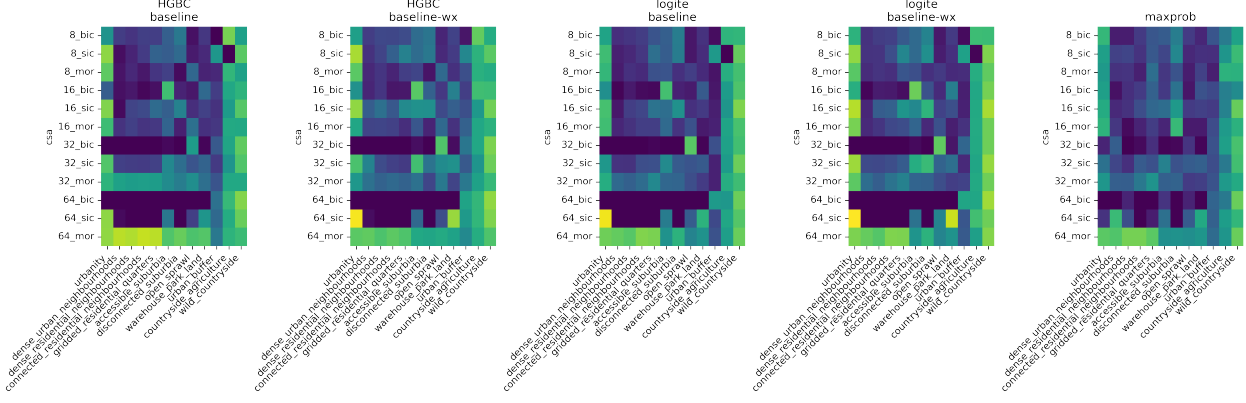


Figure 6: Within-class accuracy scores grouped by model. Each panel represents results from one of the five models compared, namely: histogram-based boosted classifier (HGBC) with features pertaining only to a given chip (**baseline**) or including also features from neighbouring ones (**baseline-wx**); Logit ensemble (**logite**) with the same two variations; and a simpler maximum probability approach (**maxprob**). Each row in the heatmap corresponds to a pair of chipsizes (8, 16, 32, and 64 pixels) and architecture (baseline image classification, or **bic**; sliding image classification, or **sic**; and multi-output regression, or **mor**) used in the neural network stage of the pipeline. Colouring is standardised across panels and values range from 0 (dark purple) to 1 (bright yellow).

	κ	Global Accuracy	Macro F1 w.	Macro F1 avg.
Intercept	0.2185*** (0.0209)	0.3236*** (0.0175)	0.2790*** (0.0174)	0.1798*** (0.0375)
(M) Logit E.	-0.0245 (0.0168)	-0.0256* (0.0141)	-0.0324** (0.0141)	-0.0325 (0.0302)
(M) Max. Prob.	-0.0559** (0.0222)	-0.0606*** (0.0187)	-0.0421** (0.0186)	-0.0296 (0.0399)
(A) M.O.R.	0.0227 (0.0184)	-0.0357** (0.0155)	-0.0278* (0.0154)	0.1787*** (0.0331)
(A) S.I.C.	0.0232 (0.0184)	-0.0247 (0.0155)	-0.0171 (0.0154)	0.1101*** (0.0331)
Chip Size	0.0036*** (0.0004)	0.0043*** (0.0003)	0.0048*** (0.0003)	0.0014** (0.0006)
W	0.0572*** (0.0168)	0.0468*** (0.0141)	0.0531*** (0.0141)	0.0392 (0.0302)
R^2	0.7214	0.8281	0.8514	0.4191
R^2 Adj.	0.6899	0.8086	0.8346	0.3533
N.	60	60	60	60

Table 3: Regression outputs explaining global non-spatial performance scores. Explanatory variables with a preceding (M) and (A) correspond to binary variables for the type of model (with histogram-based boosted classifier, or HGBC, as the baseline) and architecture (with baseline image classification, or BIC, as the baseline), respectively. Standard errors in parenthesis. Coefficients significant at the 1%, 5%, 10% level are noted with ***, **, and *, respectively.

Regression outputs for within-class accuracy

Table 4 then looks again at the within-class accuracy explaining what we have seen in Figure 6. Multi-output regression consistently outperforms both baseline image classification and sliding image classification (which shows inconsistent results itself). Chip size has, again, a positive effect on the performance, while the inclusion of spatial lag in the modelling also consistently shows a positive impact. As assumed above, the prediction of signature types on both extremes of the urban-wild range tends to be easier than classes in between, which are, conceptually, the most challenging to predict due to the higher amount of *transition land* between class core areas.

Regression outputs for spatial performance metrics

The regression outputs explaining differences in the spatial pattern between observed and predicted values measured by the Join Counts statistic offer another - spatially explicit - perspective on the performance of tested model configurations. As such, it also indicates slightly different results as presented in Table 5. Neither option of the probability modelling steps seem to have a significant effect on the Join Counts results, unlike in previous performance metrics. However, the architecture of the neural network step shows a significant effect as multi-output regression, and in two out of four cases also sliding image classification, outperform the baseline image classification. While the effect of the chip size is inconsistent across the options, the inclusion of the spatial lag in the modelling step has a significant effect (at either 10%, 5% or 1% significance level). The effect of a signature type depends on its nature. More compact urban types like *Urbanity* and *Dense urban neighbourhoods* show significance when using a distance threshold spatial weights, while sparser signature types like *Open Sprawl* and *Urban Buffer* show significance when using a union of weights.

4. Discussion and conclusion

The results can be summarised in four dimensions. The first dimension tested is the way of chip sampling and related CNN architecture. It seems clear that the baseline image classification is limited, and either the sliding approach to minimise the disbalance of sample size per class or multi-output regression shall be preferred in a use case like signature detection. Of the two, multi-output regression even seems to be better, and one of the reasons could be its ability to implicitly capture co-location. While BIC and SIC-based models have no information on the geographical relationship between neighbouring signature types, MOR directly captures these as chips often cross multiple signature types. This behaviour is unique to geographical problems. Aspatial image classification tasks are not able to encode *distance* between two types in this way. The second dimension is the chip size. Except for Join Counts statistics, we see a positive relationship between model performance and the extent our chips cover. This is an expected outcome as the larger the chip is, the more information it contains. However, we cannot blindly follow *larger is better* logic as signature types are composed of granular geometries, and we see a sampling issue when the chip size grows. While that can be partially mitigated by using MOR

Within-Class Accuracy	Baseline	Absolute imb.	Relative imb.
Intercept	0.1866*** (0.0308)	-0.0237 (0.0311)	0.0595** (0.0303)
(M) Logit E.	-0.0125 (0.0159)	-0.0125 (0.0141)	-0.0125 (0.0146)
(M) Max. Prob.	-0.0188 (0.0211)	-0.0188 (0.0186)	-0.0188 (0.0193)
(A) M.O.R.	0.1753*** (0.0175)	0.2512*** (0.0163)	0.1753*** (0.0160)
(A) S.I.C.	0.1202*** (0.0175)	-0.0783*** (0.0209)	0.1202*** (0.0160)
Chip Size	0.0014*** (0.0003)	0.0041*** (0.0003)	0.0014*** (0.0003)
1k Obs.		0.0514*** (0.0036)	
% Obs.			0.0156*** (0.0013)
W	0.0365** (0.0159)	0.0365*** (0.0141)	0.0365** (0.0146)
(S)Urbanity	0.2358*** (0.0349)	0.2022*** (0.0309)	0.2574*** (0.0320)
(S)Dense urban neighbourhoods	-0.1420*** (0.0349)	-0.1075*** (0.0309)	-0.0998*** (0.0322)
(S)Dense residential neighbourhoods	-0.1414*** (0.0349)	-0.0836*** (0.0311)	-0.0983*** (0.0322)
(S)Connected residential neighbourhoods	-0.1306*** (0.0349)	-0.0726** (0.0311)	-0.0754** (0.0323)
(S)Gridded residential quarters	-0.0785** (0.0349)	-0.0127 (0.0312)	-0.0049 (0.0326)
(S)Disconnected suburbia	-0.0601* (0.0349)	-0.0103 (0.0311)	-0.0019 (0.0324)
(S)Open sprawl	-0.0845** (0.0349)	-0.0995*** (0.0309)	-0.1143*** (0.0321)
(S)Warehouse park land	-0.0857** (0.0349)	-0.0788** (0.0309)	-0.0817** (0.0320)
(S)Urban buffer	-0.0828** (0.0349)	-0.1382*** (0.0311)	-0.1753*** (0.0330)
(S)Countryside agriculture	0.2236*** (0.0349)	0.1593*** (0.0312)	0.1118*** (0.0334)
(S)Wild countryside	0.3876*** (0.0349)	0.3283*** (0.0311)	0.2925*** (0.0330)
R^2	0.4979	0.6087	0.5794
R^2 Adj.	0.4857	0.5987	0.5686
N.	720	720	720

Table 4: Regression outputs explaining within-class accuracy. Explanatory variables with a preceding (M), (A) and (S) correspond to binary variables for the type of model (with histogram-based boosted classifier, or HGBC, as the baseline), architecture (with baseline image classification, or BIC, as the baseline) and spatial signature (with Accessible suburbia as the baseline), respectively. Standard errors in parenthesis. Coefficients significant at the 1%, 5%, 10% level are noted with ***, **, and *, respectively.

	JC W_thr	$\log(JC)$ W_thr	JC W_union	$\log(JC)$ W_union
Intercept	4.3454*** (0.9507)	1.4617*** (0.1344)	4.7103*** (0.5763)	1.6311*** (0.1080)
(M) Logit E.	-0.1406 (0.4951)	-0.0431 (0.0700)	0.1851 (0.2995)	0.0481 (0.0561)
(M) Max. Prob.	0.1128 (0.6442)	-0.1223 (0.0911)	0.2819 (0.3887)	0.0223 (0.0728)
(A) M.O.R.	-3.1630*** (0.5494)	-0.5744*** (0.0777)	-2.7875*** (0.3301)	-0.4647*** (0.0619)
(A) S.I.C.	0.0119 (0.5532)	-0.2390*** (0.0782)	-0.6666** (0.3329)	-0.0481 (0.0624)
Chip Size	0.0297*** (0.0108)	-0.0005 (0.0015)	-0.0061 (0.0065)	-0.0080*** (0.0012)
W	-0.9325* (0.4945)	-0.1376** (0.0699)	-0.9556*** (0.2991)	-0.1785*** (0.0560)
(S)Urbanity	4.6650*** (1.0696)	0.6574*** (0.1512)	0.1156 (0.6460)	-0.1258 (0.1211)
(S)Dense urban neighbourhoods	1.7796* (1.0695)	0.5094*** (0.1512)	0.7480 (0.6487)	0.1609 (0.1216)
(S)Dense residential neighbourhoods	-0.8545 (1.0958)	0.0672 (0.1550)	-0.4636 (0.6647)	-0.0920 (0.1246)
(S)Connected residential neighbourhoods	-0.3656 (1.1018)	0.1543 (0.1558)	-0.4388 (0.6647)	-0.1447 (0.1246)
(S)Gridded residential quarters	-0.2000 (1.0744)	0.1009 (0.1519)	-0.6203 (0.6517)	-0.2111* (0.1221)
(S)Disconnected suburbia	-0.9752 (1.1213)	-0.1719 (0.1586)	-1.0303 (0.6684)	-0.3358*** (0.1252)
(S)Open sprawl	1.8342* (1.0604)	0.1734 (0.1499)	2.1575*** (0.6432)	0.3576*** (0.1205)
(S)Warehouse park land	0.5496 (1.0694)	0.2123 (0.1512)	1.2245* (0.6487)	0.3054** (0.1216)
(S)Urban buffer	-0.0558 (1.0521)	-0.0931 (0.1488)	2.7027*** (0.6382)	0.5164*** (0.1196)
(S)Countryside agriculture	-1.3759 (1.0521)	-0.2511* (0.1488)	0.6623 (0.6382)	0.0670 (0.1196)
(S)Wild countryside	-2.0183* (1.0521)	-0.5065*** (0.1488)	-0.5918 (0.6382)	-0.1635 (0.1196)
R^2	0.1589	0.1954	0.2118	0.2660
R^2 Adj.	0.1368	0.1743	0.1913	0.2468
N.	665	665	670	670

Table 5: Regression outputs explaining (log of) differences in the spatial pattern between observed and predicted values, as measured by the Join Counts statistic. The Join Counts for each signature were computed using two types of spatial weights: one based on a distance threshold of 1Km (W_thr), and another one built as a the union of nearest neighbor and queen contiguity matrices (W_union). Explanatory variables with a preceding (M), (A) and (S) correspond to binary variables for the type of model (with histogram-based boosted classifier, or HGBC, as the baseline), architecture (with baseline image classification, or BIC, as the baseline) and spatial signature (with Accessible suburbia as the baseline), respectively. Standard errors in parenthesis. Coefficients significant at the 1%, 5%, 10% level are noted with ***, **, and *, respectively.

for single-class prediction, it needs to be considered in model architecture. Another dimension looks at the value of modelling on top of probabilities coming from neural networks. The results indicate that there is value in the modelling step as the maximum probability option, used as a default if no modelling is employed, tends to underperform both logit models and histogram-based gradient boosted classifiers. While the difference between logit and HGBC is not always significant, some results suggest that the non-linear nature of HGBC provides better performance than linear logit models. The last dimension focuses on the inclusion of the spatial lag in the modelling step as a geographically-explicit method of capturing the context of each chip. This has one of the most consistent effects on performance indicating the models that exclude spatial lag have worse results than those that include it. Yet again, this step would not be possible in an aspatial image classification context where two samples have no “spatial” distance from each other hence no spatial weights matrix can be created. This is a clear evidence of the value of explicitly spatial modelling in this context, and we can only recommend wider adoption of such methods. Combining all the dimensions, we can assume that the optimal model for the detection of spatial signatures from Sentinel 2 satellite imagery should define CNN for the multi-output regression problem based on larger chip size and passing the output to non-linear probability modelling with a spatial lag component.

Regardless of global performance, we cannot assume that even the best model will perform evenly across all 12 signature types. The within-class performance metrics indicate that some classes on the extreme sides of the urban-rural dimension are easier to detect. That is not surprising as both *Urbanity* and *Wild countryside* signature types are unique, while the difference between *Dense residential neighbourhoods* and *Connected residential neighbourhoods* that is visible on the satellite imagery is much more subtle. It is also common that some of the classes are easier to distinguish than others (Zanaga et al. (2021), Karra et al. (2021)). However, any model deployed for periodical updates of signature classification will have to deal with this limitation.

The experiments presented in this article focus on specific target data represented by spatial signatures. Because the signatures are designed to capture the structure of urban environments, the behaviour of spatial components in the modelling pipeline may differ when target data are of a different nature. However, we argue that the principle still holds in most cases as the uniqueness of satellite data in image classification is well recognised and will generally offer specific solutions unavailable when the task is aspatial.

Since this article is restricted to the use of open data at every step, the best current resolution of satellite imagery is 10 meters per pixel, as offered by the Sentinel 2 mission. That poses some challenges because such a resolution limits the amount of information we can capture on a small area and may oversimplify urban environments that are naturally more granular in their patterns than what 10m can capture. Further research should explore the performance differences when very-high-resolution imagery is used instead.

The combination of signatures reflecting small-scale urban types and a relatively coarse resolution leads to another limitation this work faces - the struggle to sample chips in a balanced manner. This is most prominent in the baseline image classification problem, where no pixels are shared among chips and all chips need to be exclusive to a single signature type. The issue is

alleviated by class weights in the neural network architecture, but such a solution is not optimal.

Is geography relevant in image classification problems, then? The results presented above suggest so. An introduction of explicit geographical methods to improve image classification models based on spatial imagery proves to be beneficial and makes use of what a unique - spatial - dimension offers. It requires moving beyond traditionally used pre-trained models than have no sense of adjacency of individual chips/samples. We need to take a step towards merging GIS expertise with the one that lies in the field of AI, often based in departments of computer science rather than geography.

We can also conclude that when properly designed, deep learning models have a lot of potential in characterisation of the composition of urban landscapes, if we want to answer the question from the introduction. How well they perform varies across different signature types, meaning that it will also vary across different types of urban environments when other classification than signatures is considered. Nevertheless, we can foresee a variety of applications of models of the sort presented and tested in this article. The spatial signatures are based on a large number of data sources with limited temporal rate of updates (notably census data, updated every 10 years), making it nearly impossible to do yearly snapshots of classification allowing longitudinal studies of evolution of cities. With the classification derived from satellite imagery, we can expect to see a much higher temporal resolution, easily resulting in annual updates, providing a detailed insight into the dynamics of urban expansion, densification and overall change of the shape of cities. This is a potential application that is not limited to spatial signatures but can be extended to any classification of urban environments.

When using openly available satellite data that are currently limited to the resolution of 10 meters per pixel at best, and classification focusing on primarily urban landscape, our results show both potential and limits. Accuracy is not far from that of established LULC models that could be increased in future by expansion of the training data set and possible inclusion of other available bands (like near-infrared) in the model. A limitation in decreased performance when it comes to distinction between urban areas that are neither too dense nor too sparse but show different form and function profiles. It is either a difference that is not visible on imagery (e.g. more driven by function) or a limitation of the available resolution and / or training data volume. This issue could have been primarily driven by the nature of spatial signatures as a classification target, and it shall be tested on other types of urban classification in the future.

While satellite imagery and neural networks have been around for some time already, we are just entering the era of an increasing abundance of satellite-based data. What used to be reserved for national agencies and international consortia is becoming a domain of commercial subjects. Research in the remote sensing area will face not a lack of available data but the opposite. We may find ourselves in a situation where a vast amount of data streams will come our way, but we will struggle to make sense of it. We believe that the research presented in this article helps in finding our way through.

Data and code availability statement

All the data and code will be available on a public repository with DOI upon acceptance of the article to ensure anonymity of a double-blind review.

References

- Arribas-Bel, D. and Fleischmann, M. (2022). Spatial signatures - understanding (urban) spaces through form and function. *Habitat International*, 128:102641.
- Brown, C. F., Brumby, S. P., Guzder-Williams, B., Birch, T., Hyde, S. B., Mazzariello, J., Czerwinski, W., Pasquarella, V. J., Haertel, R., Ilyushchenko, S., et al. (2022). Dynamic world, near real-time global 10 m land use land cover mapping. *Scientific Data*, 9(1):1–17.
- Cliff, A. D. and Ord, J. K. (1981). *Spatial processes: models & applications*. Taylor & Francis.
- Cohen, J. (1960). A coefficient of agreement for nominal scales. *Educational and psychological measurement*, 20(1):37–46.
- Corbane, C., Politis, P., Kempeneers, P., Simonetti, D., Soille, P., Burger, A., Pesaresi, M., Sabo, F., Syrris, V., and Kemper, T. (2020). A global cloud free pixel- based image composite from sentinel-2 data. *Data in Brief*, 31:105737.
- Deng, J., Dong, W., Socher, R., Li, L.-J., Li, K., and Fei-Fei, L. (2009). Imagenet: A large-scale hierarchical image database. In *2009 IEEE conference on computer vision and pattern recognition*, pages 248–255. Ieee.
- Dijkstra, L., Florczyk, A. J., Freire, S., Kemper, T., Melchiorri, M., Pesaresi, M., and Schiavina, M. (2021). Applying the degree of urbanisation to the globe: A new harmonised definition reveals a different picture of global urbanisation. *Journal of Urban Economics*, 125:103312. Delineation of Urban Areas.
- European Environment Agency (1990). CORINE Land Cover. pages 1–163.
- European Environment Agency and European Environment Agency (2020). Urban atlas land cover/land use 2018 (vector), europe, 6-yearly, jul. 2021.
- Fleischmann, M. and Arribas-Bel, D. (2022). Geographical characterisation of british urban form and function using the spatial signatures framework. *Scientific Data*, 9(546):1–15.
- He, K., Zhang, X., Ren, S., and Sun, J. (2016). Deep residual learning for image recognition. In *Proceedings of the IEEE conference on computer vision and pattern recognition*, pages 770–778.
- Izzo, S., Prezioso, E., Giampaolo, F., Mele, V., Di Somma, V., and Mei, G. (2022). Classification of urban functional zones through deep learning. *Neural Computing and Applications*, 34(9):6973–6990.
- Jing, Y., Sun, R., and Chen, L. (2022). A method for identifying urban functional zones based on landscape types and human activities. *Sustainability*, 14(7):4130.
- Karra, K., Kontgis, C., Statman-Weil, Z., Mazzariello, J. C., Mathis, M., and Brumby, S. P. (2021). Global land use/land cover with sentinel 2 and deep learning. In *2021 IEEE international geoscience and remote sensing symposium IGARSS*, pages 4704–4707. IEEE.
- Ke, G., Meng, Q., Finley, T., Wang, T., Chen, W., Ma, W., Ye, Q., and Liu, T.-Y. (2017). Lightgbm: A highly efficient gradient boosting decision tree. *Advances in neural information processing systems*, 30.
- Ke, Y. and Quackenbush, L. J. (2011). A review of methods for automatic individual tree-crown detection and delineation from passive remote sensing. *International Journal of Remote Sensing*, 32(17):4725–4747.

- Koc, C. B., Osmond, P., Peters, A., and Irger, M. (2017). Mapping local climate zones for urban morphology classification based on airborne remote sensing data. In *2017 Joint Urban Remote Sensing Event (JURSE)*, pages 1–4. IEEE.
- Kuffer, M., Grippa, T., Persello, C., Taubenböck, H., Pfeffer, K., and Sliuzas, R. (2021). Mapping the morphology of urban deprivation: The role of remote sensing for developing a global slum repository. *Urban Remote Sensing: Monitoring, Synthesis, and Modeling in the Urban Environment*, pages 305–323.
- Kuffer, M., Pfeffer, K., and Sliuzas, R. (2016). Slums from space - 15 years of slum mapping using remote sensing. *Remote Sensing*, 8(6):455.
- Lai, F., Sharma, A., Liu, X., and Yang, X. (2021). Deep learning for urban and landscape mapping from remotely sensed imagery. *Urban Remote Sensing: Monitoring, Synthesis, and Modeling in the Urban Environment*, pages 153–174.
- LeCun, Y., Bengio, Y., and Hinton, G. (2015). Deep learning. *nature*, 521(7553):436–444.
- Liu, S. and Shi, Q. (2020). Local climate zone mapping as remote sensing scene classification using deep learning: A case study of metropolitan china. *ISPRS Journal of Photogrammetry and Remote Sensing*, 164:229–242.
- Longley, P. A. (2002). Geographical information systems: will developments in urban remote sensing and gis lead to 'better' urban geography? *Progress in Human Geography*, 26(2):231–239.
- Lu, W., Qi, J., and Feng, H. (2022). Urban functional zone classification based on self-supervised learning: A case study in beijing, china. *Frontiers in Environmental Science*, 10:1010630.
- Microsoft (2019). USBuildingFootprints. <https://github.com/Microsoft/USBuildingFootprints>.
- Openshaw, S. (1981). The modifiable areal unit problem. *Quantitative geography: A British view*, pages 60–69.
- Othman, E., Bazi, Y., Melgani, F., Alhichri, H., Alajlan, N., and Zuaire, M. (2017). Domain adaptation network for cross-scene classification. *IEEE Transactions on Geoscience and Remote Sensing*, 55(8):4441–4456.
- Pedregosa, F., Varoquaux, G., Gramfort, A., Michel, V., Thirion, B., Grisel, O., Blondel, M., Prettenhofer, P., Weiss, R., Dubourg, V., et al. (2011). Scikit-learn: Machine learning in python. *the Journal of machine Learning research*, 12:2825–2830.
- Qiu, C., Mou, L., Schmitt, M., and Zhu, X. X. (2020). Fusing multiseasonal sentinel-2 imagery for urban land cover classification with multibranch residual convolutional neural networks. *IEEE Geoscience and Remote Sensing Letters*, 17(10):1787–1791.
- Rashed, T. and Jürgens, C. (2010). *Remote sensing of urban and suburban areas*, volume 10. Springer Science & Business Media.
- Ronneberger, O., Fischer, P., and Brox, T. (2015). U-net: Convolutional networks for biomedical image segmentation. In *International Conference on Medical image computing and computer-assisted intervention*, pages 234–241. Springer.
- Russakovsky, O., Deng, J., Su, H., Krause, J., Satheesh, S., Ma, S., Huang, Z., Karpathy, A., Khosla, A., Bernstein, M., Berg, A. C., and Fei-Fei, L. (2015). ImageNet Large Scale Visual Recognition Challenge. *International Journal of Computer Vision (IJCV)*, 115(3):211–252.

- Sharma, A., Liu, X., Yang, X., and Shi, D. (2017). A patch-based convolutional neural network for remote sensing image classification. *Neural Networks*, 95:19–28.
- Simonyan, K. and Zisserman, A. (2014). Very deep convolutional networks for large-scale image recognition. *arXiv preprint arXiv:1409.1556*.
- Srivastava, S., Vargas-Munoz, J. E., and Tuia, D. (2019). Understanding urban landuse from the above and ground perspectives: A deep learning, multimodal solution. *Remote sensing of environment*, 228:129–143.
- Stewart, I. D. and Oke, T. R. (2012). Local Climate Zones for Urban Temperature Studies. *Bulletin of the American Meteorological Society*, 93(12):1879–1900.
- Tan, M. and Le, Q. V. (2019). Efficientnet: Rethinking model scaling for convolutional neural networks.
- Taubenböck, H., Debray, H., Qiu, C., Schmitt, M., Wang, Y., and Zhu, X. (2020). Seven city types representing morphologic configurations of cities across the globe. *Cities*, 105:102814.
- Venter, Z. S., Barton, D. N., Chakraborty, T., Simensen, T., and Singh, G. (2022). Global 10 m land use land cover datasets: A comparison of dynamic world, world cover and esri land cover. *Remote Sensing*, 14(16):4101.
- Wang, J., Fleischmann, M., Venerandi, A., Kuffer, M., and Porta, S. (2022a). *Earth observation + morphometrics: towards a systematic understanding of cities in challenging contexts*, pages 363–370. University of Strathclyde. 28th International Seminar on Urban Form, ISUF 2021, ISUF 2021 ; Conference date: 29-06-2021 Through 03-07-2021.
- Wang, J., Georganos, S., Kuffer, M., Abascal, A., and Vanhuysse, S. (2022b). On the knowledge gain of urban morphology from space. *Computers, Environment and Urban Systems*, 95:101831.
- Wang, L., Xu, X., Dong, H., Gui, R., and Pu, F. (2018a). Multi-pixel simultaneous classification of polsar image using convolutional neural networks. *Sensors*, 18(3):769.
- Wang, R., Ren, C., Xu, Y., Lau, K. K.-L., and Shi, Y. (2018b). Mapping the local climate zones of urban areas by gis-based and wudapt methods: A case study of hong kong. *Urban climate*, 24:567–576.
- Weng, Q. and Quattrochi, D. A. (2018). *Urban remote sensing*. CRC press.
- Yang, X. X. (2021). *Urban remote sensing: Monitoring, synthesis and modeling in the urban environment*. John Wiley & Sons.
- Zanaga, D., Van De Kerchove, R., De Keersmaecker, W., Souverijns, N., Brockmann, C., Quast, R., Wevers, J., Grosu, A., Paccini, A., Vergnaud, S., Cartus, O., Santoro, M., Fritz, S., Georgieva, I., Lesiv, M., Carter, S., Herold, M., Li, L., Tsendlbazar, N.-E., Ramoino, F., and Arino, O. (2021). Esa worldcover 10 m 2020 v100.
- Zhou, L., Shao, Z., Wang, S., and Huang, X. (2022). Deep learning-based local climate zone classification using sentinel-1 sar and sentinel-2 multispectral imagery. *Geo-spatial Information Science*, pages 1–16.
- Zhou, Y., Wei, T., Zhu, X., and Collin, M. (2021). A parcel-based deep-learning classification to map local climate zones from sentinel-2 images. *IEEE Journal of Selected Topics in Applied Earth Observations and Remote Sensing*, 14:4194–4204.

Zhu, X. X., Qiu, C., Hu, J., Shi, Y., Wang, Y., Schmitt, M., and Taubenböck, H. (2022). The urban morphology on our planet—global perspectives from space. *Remote Sensing of Environment*, 269:112794.

Appendix A. Technical appendix

A. Comparison of neural network architecture

architecture	top layer	# neurons in top layer	global accuracy
EfficientNetB4	Flatten	128	0.663482
EfficientNetB4	Flatten	256	0.715764
EfficientNetB4	Flatten	512	0.697187
EfficientNetB4	GlobalAveragePooling2D	128	0.723726
EfficientNetB4	GlobalAveragePooling2D	256	0.715764
EfficientNetB4	GlobalAveragePooling2D	512	0.727972
ResnNet50	Flatten	128	0.481157
ResnNet50	Flatten	256	0.481423
ResnNet50	Flatten	512	0.522824
ResnNet50	GlobalAveragePooling2D	128	0.469745
ResnNet50	GlobalAveragePooling2D	256	0.469745
ResnNet50	GlobalAveragePooling2D	512	0.526274
VGG19	Flatten	128	0.708333
VGG19	Flatten	256	0.675425
VGG19	Flatten	512	0.692144
VGG19	GlobalAveragePooling2D	128	0.69931
VGG19	GlobalAveragePooling2D	256	0.678609
VGG19	GlobalAveragePooling2D	512	0.67224

Table 6: Comparison of global accuracy of different architectures of neural network on a sample of data with signature types aggregated into three classes (centres, periphery, countryside) using the baseline image classification. EfficientNetB4 with GlobalAveragePooling2D and 256 neurons has been used in the final experiment.

B. Within-class performance by spatial signature

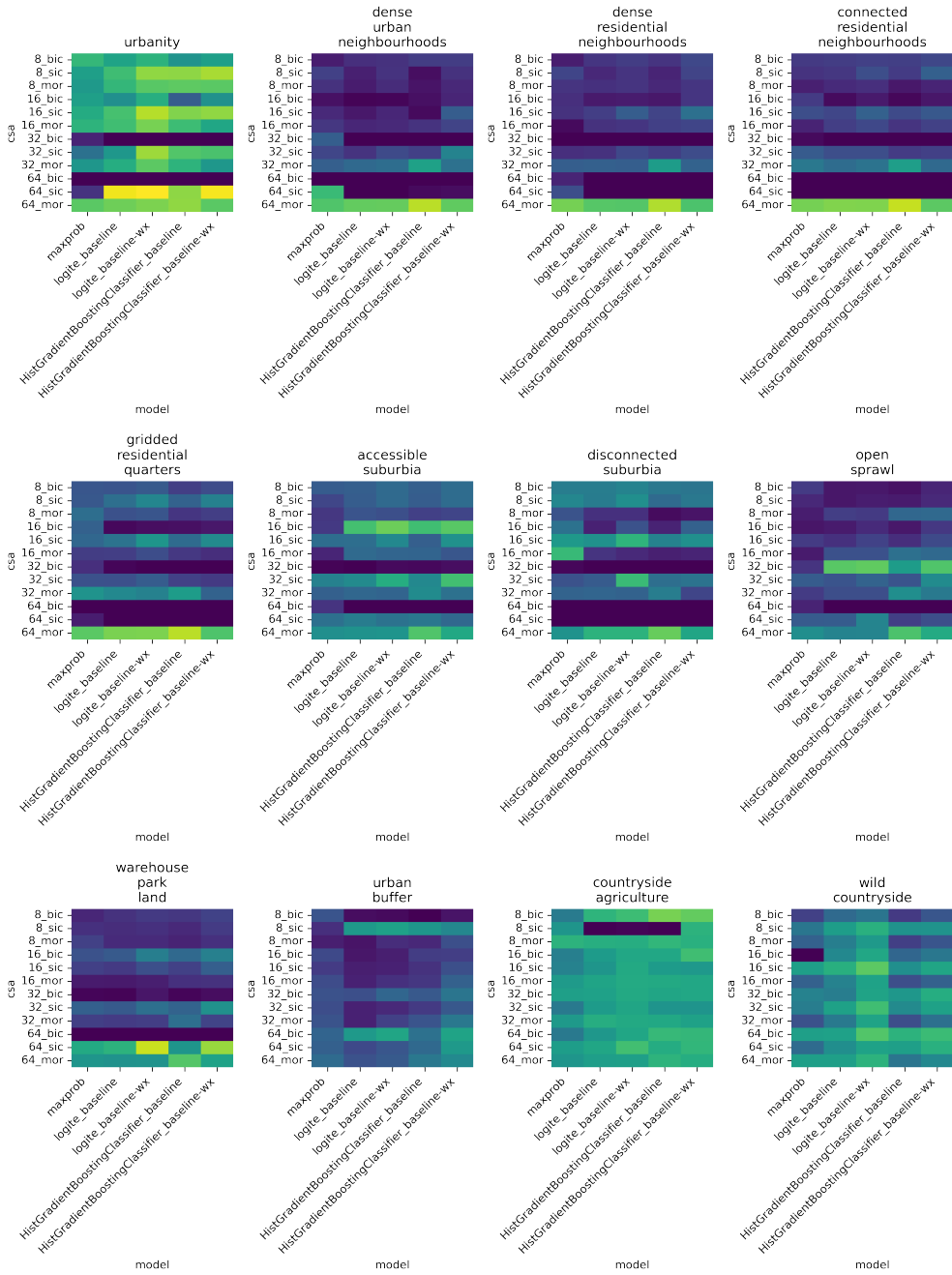


Figure 7: Within-class accuracy scores grouped by signature. Each panel represents results from one of the 12 signatures predicted. Each column in the heatmap corresponds to one of the five models compared, namely: histogram-based boosted classifier (HGBC) with features pertaining only to a given chip (baseline) or including also features from neighbouring ones (baseline-wx); Logit ensemble (logite) with the same two variations; and a simpler maximum probability approach (maxprob). Each row corresponds to a pair of chipsizes (8, 16, 32, and 64 pixels) and architecture (baseline image classification, or bic; sliding image classification, or sic; and multi-output regression, or mor) used in the neural network stage of the pipeline.

C. Confusion matrices

D. Fit of chips within signature types

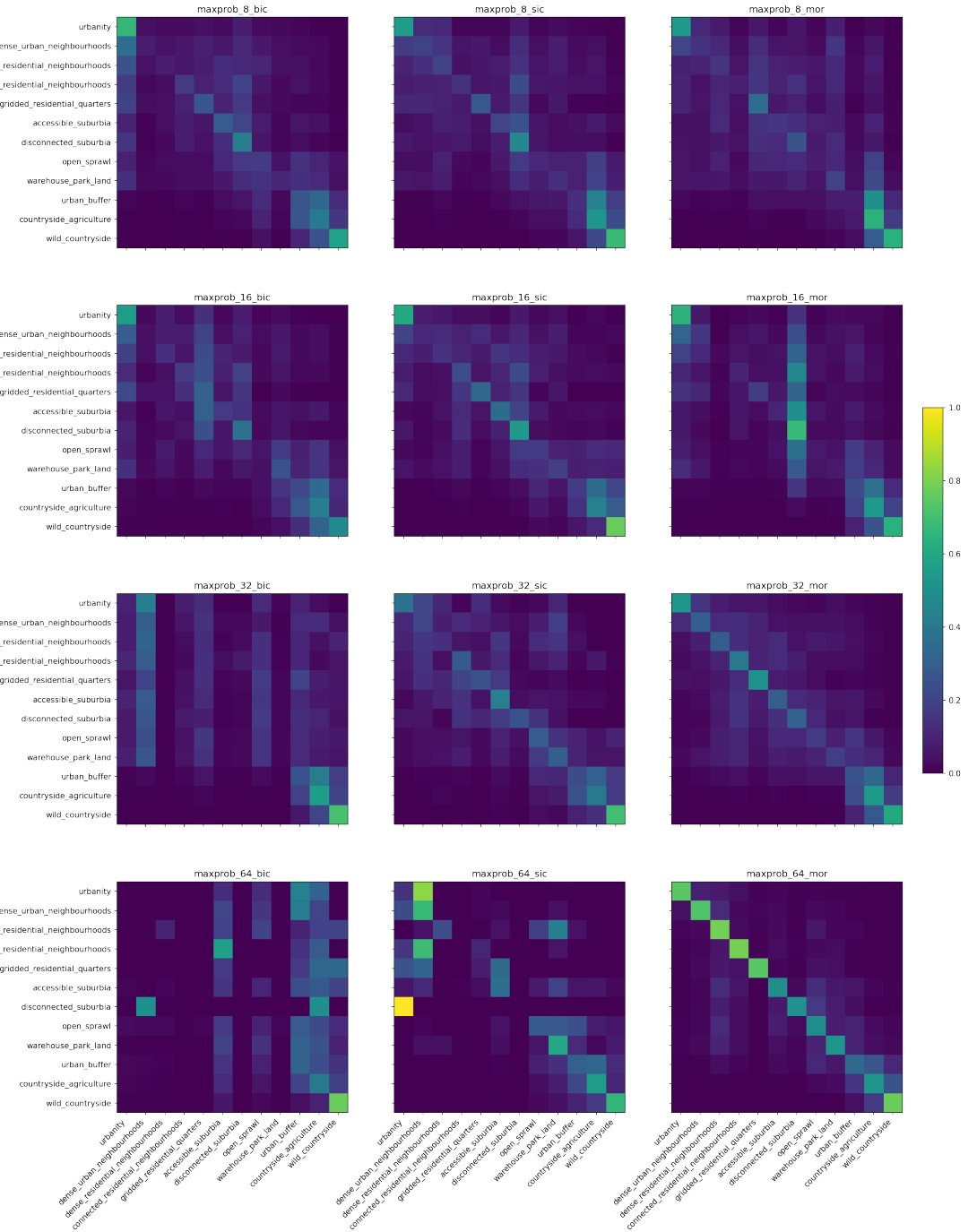


Figure 8: Confusion matrices for individual models denoting the ability of each model in prediction of a correct label per each class using the maximum probability architecture.

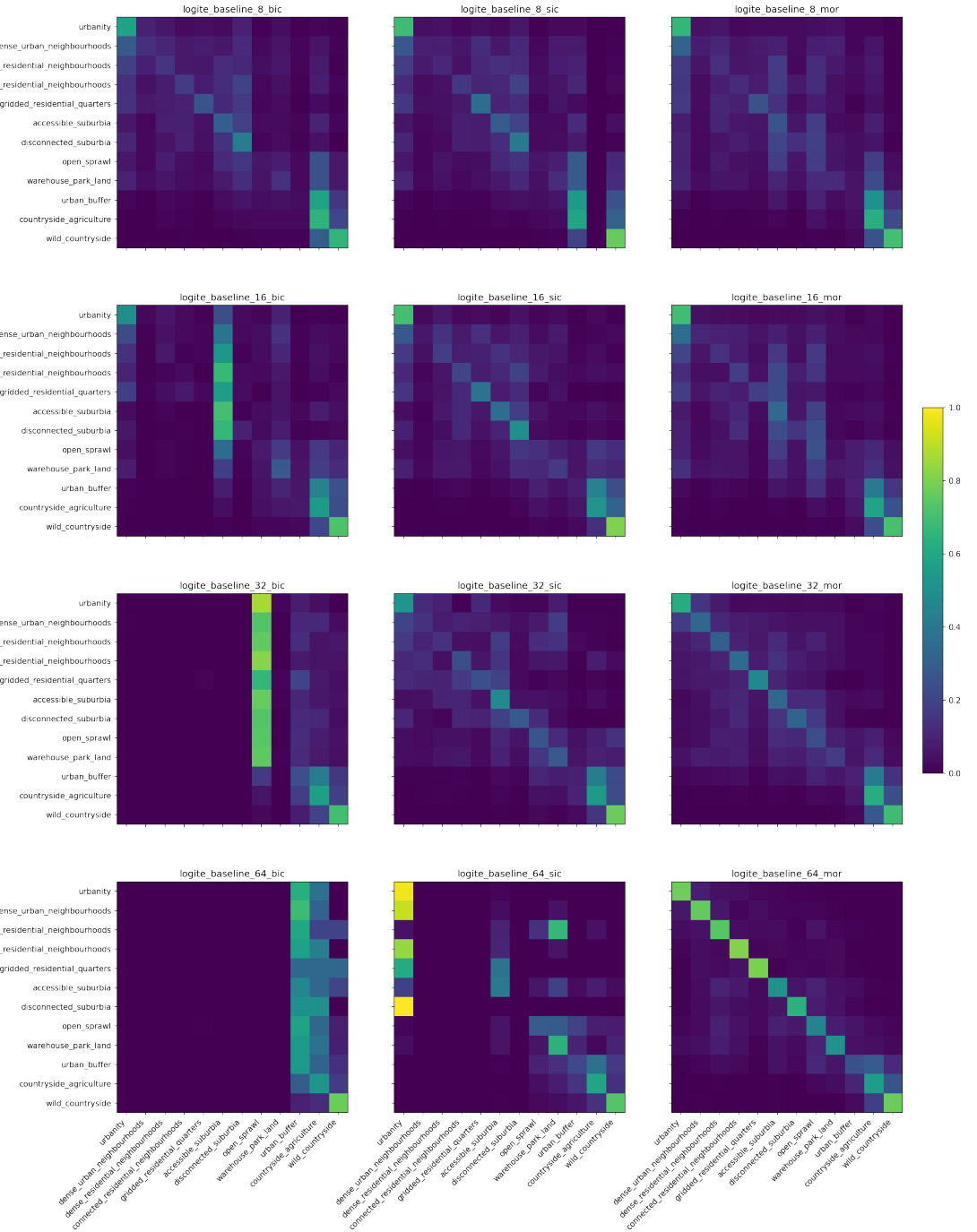


Figure 9: Confusion matrices for individual models denoting the ability of each model in prediction of a correct label per each class using the logit ensemble baseline architecture.

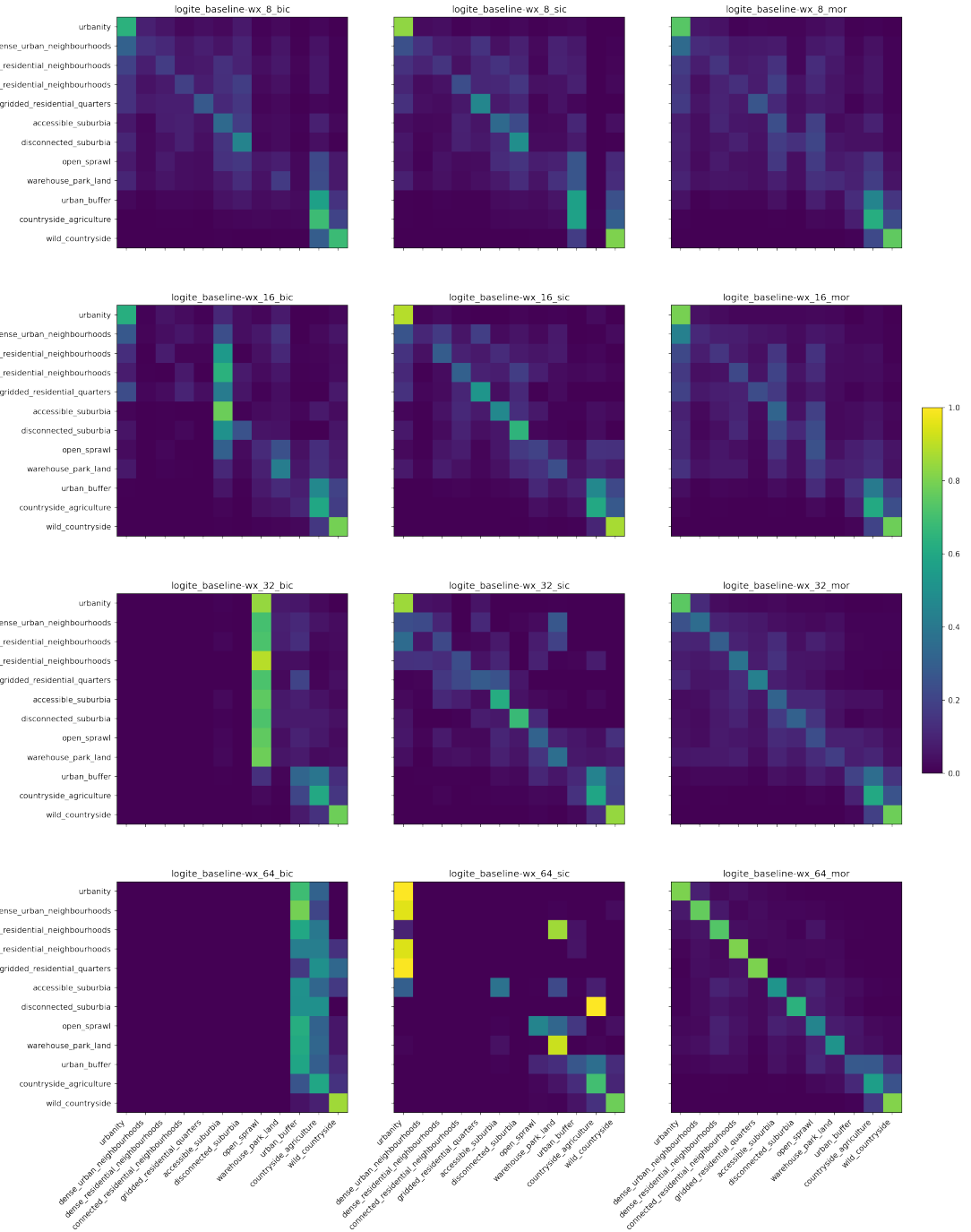


Figure 10: Confusion matrices for individual models denoting the ability of each model in prediction of a correct label per each class using the logit ensemble baseline-wx architecture.

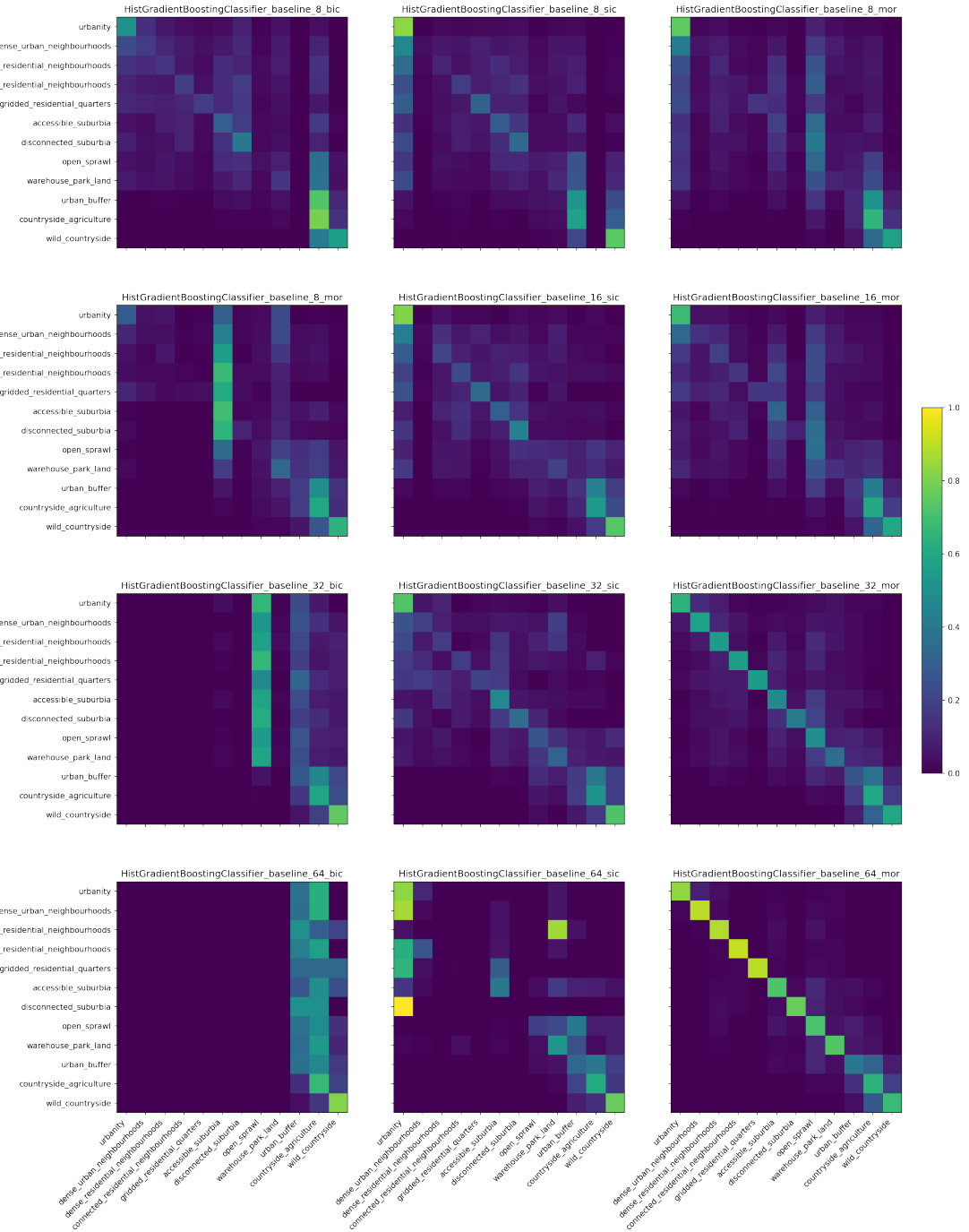


Figure 11: Confusion matrices for individual models denoting the ability of each model in prediction of a correct label per each class using the HGBC baseline architecture.

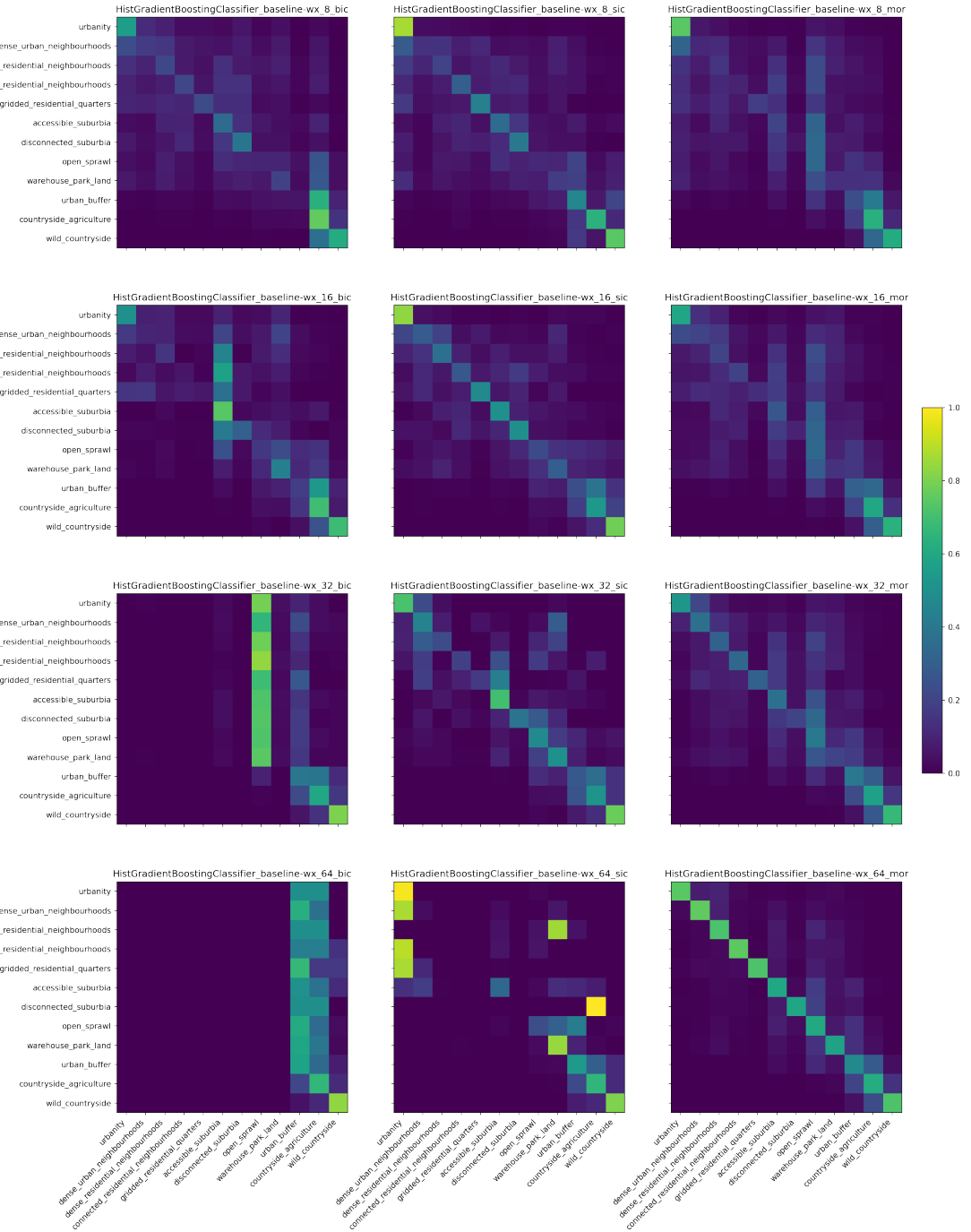


Figure 12: Confusion matrices for individual models denoting the ability of each model in prediction of a correct label per each class using the HGBC baseline-wx architecture.

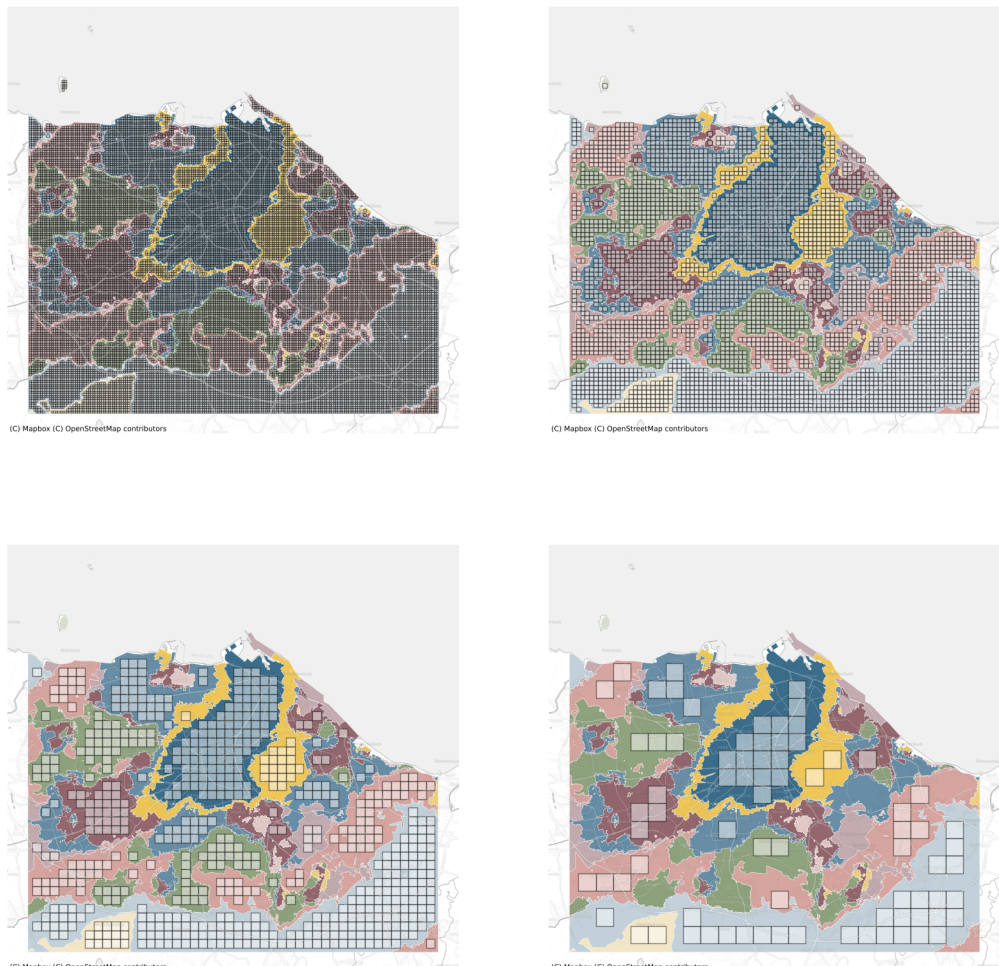


Figure 13: An illustration of the relationship between chip size and signature geometry in Edinburgh area. Subplots show all chips that represent a single class using 80 meters (top left), 160 m (top right), 320 m (bottom left) and 640 m (bottom right) chip sizes.

	B.I.C.	S.I.C	M.O.R.
8	534,729	1,099,439	135,264
16	331,459	1,087,827	126,016
32	179,261	901,538	112,196
64	132,619	373,131	94,960

Table 7: Total number of chips (within all training, validation and secret sets) per chip size and architecture.

E. Chip counts